Dense point cloud acquisition with a low-cost Velodyne VLP-16

Jason Bula[1], Marc-Henri Derron[2], and Gregoire Mariethoz[1]

[1]University of Lausanne, Institute of Earth Surface Dynamics
[1]University of Lausanne, Institute of Earth Sciences

Abstract. This study develops a method to acquire dense point clouds with a low-cost Velodyne VLP-16 lidar system, without using expensive GNSS positioning or IMU. Our setting consists in mounting the lidar on a motor to continuously change the scan direction, which leads to a significant increase in the point cloud density. A post-treatment reconstructs the position of each point accounting for the motor angle at the time of acquisition, and a calibration step accounts for inaccuracies in the

5 hardware assemblage. The system is tested in indoors settings such as buildings and abandoned mines, but is also expected to give good results outdoors. It is also compared with a more expensive system based on IMU registration and a SLAM algorithm. The alignment between acquisitions with those two systems is within a distance of 2 cm.

1   Introduction

In the last years, sensor enhancements and the development of new platforms have led to an increased use of 3D data acquisition

10 techniques. Lidar (light detection and ranging) is an active sensor that uses the principle of time of flight to measure the distance between the sensor and the intended target to produce a 3D point cloud. The first models were atmospheric lidars launched in the 1960s. Those were used to characterize clouds (Northend et al,. 1966; Davis, 1969) or to quantify of aerosols (Schuster, 1970). Afterwards, terrestrial lidars (TLS) have been developed to measure hard targets (Ackermann, 1999) for static or mobile systems and for high-resolution modeling. Common applications include civil engineering (Barnea et Filin, 2008), management

15 of environmental hazards like landslide or rock fall (Jaboyedoff et al., 2011, 2012; Royán et al., 2014; Teza et al., 2007), or the acquisition of topographic data (Shan et Toth, 2018).

Despite a clear potential, the use of lidar is often limited by the high cost of data acquisition. Over the last decade, low-cost lidars have been launched, but those models have generally limited performance compared to the high-cost lidars. New low-cost lidar generally use rotational mirror that increase the number of scanning line and thus measure more points per second

20 (Shakleton et al., 2010). Their range is generally less than 200 meters and the resolution of the resulting point clouds is low. However, these new systems often allow very high speed data acquisition comparable to high-cost devices. In addition, low-cost lidars are very compact and therefore quick to set up in the field. This makes them promising tools in terms of efficiency (Wang et al., 2018). Such low-cost sensors are mainly used for self-driving cars (Geiger et al., 2012) or for UAV-based surveys. They typically provide a level of accuracy of the order to 5-15 cm (Stöcker et al,. 2017; Laurent et al,. 2019). Low-cost lidars

25 are widely used in robotics for obstacle avoidance for instance, but more rarely for mapping because such systems do not produce dense point cloud.

The objective of this study is to develop a method to effectively use the data produced by a low-cost lidar (Velodyne VPL-16 which can scan continuously and takes 10 frames per second) in order to produce a dense point cloud while avoiding high-cost equipment. The idea of our approach is to continuously rotate the lidar along the axis of lowest beam density. With a slow controlled rotating movement and a continuous acquisition mode, it is possible to densify the acquired point cloud such that it is comparable to data obtained with higher grade systems.

The structure of this paper is as follows : section 2 presents the equipment and the constraints associated with it to produce a low-cost system. Section 3 present the methodology used to produce high-resolution scans. Section 4 presents the result of our system. Section 5 discusses the results section 6 presents some conclusions.

2 Low-cost hardware

2.1 VLP-16 Lidar

The VLP-16 model has several lasers fixed on a rotational head. The main features of the low-cost lidar can be found in table 1.

Table 1. Velodyne VLP-16

Channel	16
Wavelength	903 nm
Accuracy	±3 cm (Typical)
Measurement Range	Up to 100m
Single Return Data Points	300000 pts/s
Field of View (vertical)	30°
Angular Resolution (vertical)	2.0°
Field of View (Horizontal)	360°
Horizontal Angular Resolution	0.1° – 0.4°
Frame rate	10 fps
Weight	830 g
Dimension	Ø 103mm, H 72mm
Retail Price	$4000

Table 2. Syrp Genie

Max rotation speed	0.58 rpm (35 s for 360 degrees)
Min rotation speed	0.0025 rpm
Payload	4 kg
Hardware Interface	Bluetooth 4.0
Dimensions	91.5 x 91.5 x 46mm
Retail Price	$250
Minimum step	0.005 degree

The acquisition mode of the VLP-16 consist in 16 fixed parallel scan lines. Each scan line records 1810 points per image, which corresponds to a angular horizontal resolution of 0.2 °. Regarding the vertical resolution, the sensor is limited to a field of view of 30 degrees. The 16 scan lines imply a low vertical angular resolution of 2.0°. Figure 1b shows a typical point cloud produced by the VLP-16 and figure 1a shows a photograph of the scanned scene with the same viewing angle. This poor resolution limits the use of the VLP-16 for terrestrial scanning applications. For example the low point density makes it difficult to co-register several scans

2.2 Syrp Genie

With the purpose to have a low-cost design, we select the Syrp Genie Mini (table 2). This motorized head can rotate 360 degrees and sustain the weight of the VLP-16.

2.3 Conception and assembly of the custom scanning system

The VLP 16 is mounted on the Syrp Genie Mini, and the entire assembly is set on an ordinary tripod and connected to a computer and a power source (figure 2). Importantly, the lidar is placed vertically using an L-shaped piece, such that the vertical (low-resolution) and horizontal (high-resolution) directions are now reversed. Our goal is to use the slow rotating motion induced by the Syrp Genie Mini to densify the point cloud across the horizontal direction. A counterweight is placed on the tripod on the opposite side of the lidar to minimize stresses that can impact the rotation speed and induce an angular distortions.

3 Methodology

3.1 Post-treatment of the data

Acquisition with our system requires a number of post-treatment steps to obtain a scan that correctly represents the scene. At the beginning of the scan, the rotation speed and the time lapse between the start and the stop of the rotation are recorded.

a)

b)
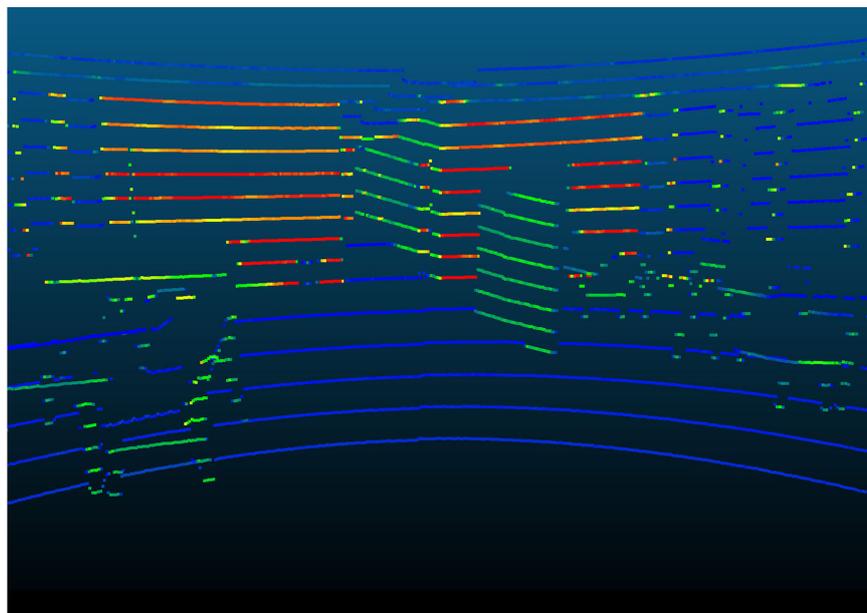
Figure 1. Typical scan created with the VLP-16, the color represents the intensity of the returned signal.

Figure 2. Terrestrial lidar system (TLS)

Then, each frame is rotated by the angle corresponding to the time of acquisition. Figure 3 takes the example of a teapot to
60   illustrate densification process, with 5 steps described below:

1. Frame at time $t = t_0$: Only a part of the teapot is scanned, corresponding to the lidar field of view (30 degrees). This
   first frame is used as reference to align the others.

2. Scan at time $t = t_1$: a second part of the teapot is scanned.

3. Representation of the scene when both frames are visible simultaneously. It is necessary to apply a transformation to
65   correctly align both frames. This transformation is equal to a rotation on the y axis in clockwise direction by an angle
   corresponding to the rotation of the motor between t_0 and t_1.

4. Image after transformation: both frames are now aligned. Frames are incrementally assembled to construct the entire
   scene.

5. Visualization of the assemblage of frames acquired between time t_0 and t_f.

70

Assuming a constant geometry of the system, we use a rigid transformation between each frame. This geometrical transfor-
mation is characterized by a 4 x 4 matrix

$$
T = \begin{bmatrix} a & b & c & 0 \\ d & e & f & 0 \\ g & h & i & 0 \\ j & k & l & 1 \end{bmatrix},
$$

with:

– abc, the rotation applied on the x-axis

75   – def the rotation applied on the y-axis,

– ghi the rotation applied on the z axis.

– jkl the translation applied on x, y and z.

In our case, the rotation is applied around the y-axis, the transformation matrix that aligns each frame is equal to:

$$
T_1 = \begin{bmatrix} (cos(\beta) & 0 & sin(\beta) & 0 \\ 0 & 1 & 0 & 0 \\ -sin(\beta) & 0 & cos(\beta) & 0 \\ 0 & 0 & 0 & 1 \end{bmatrix},
$$
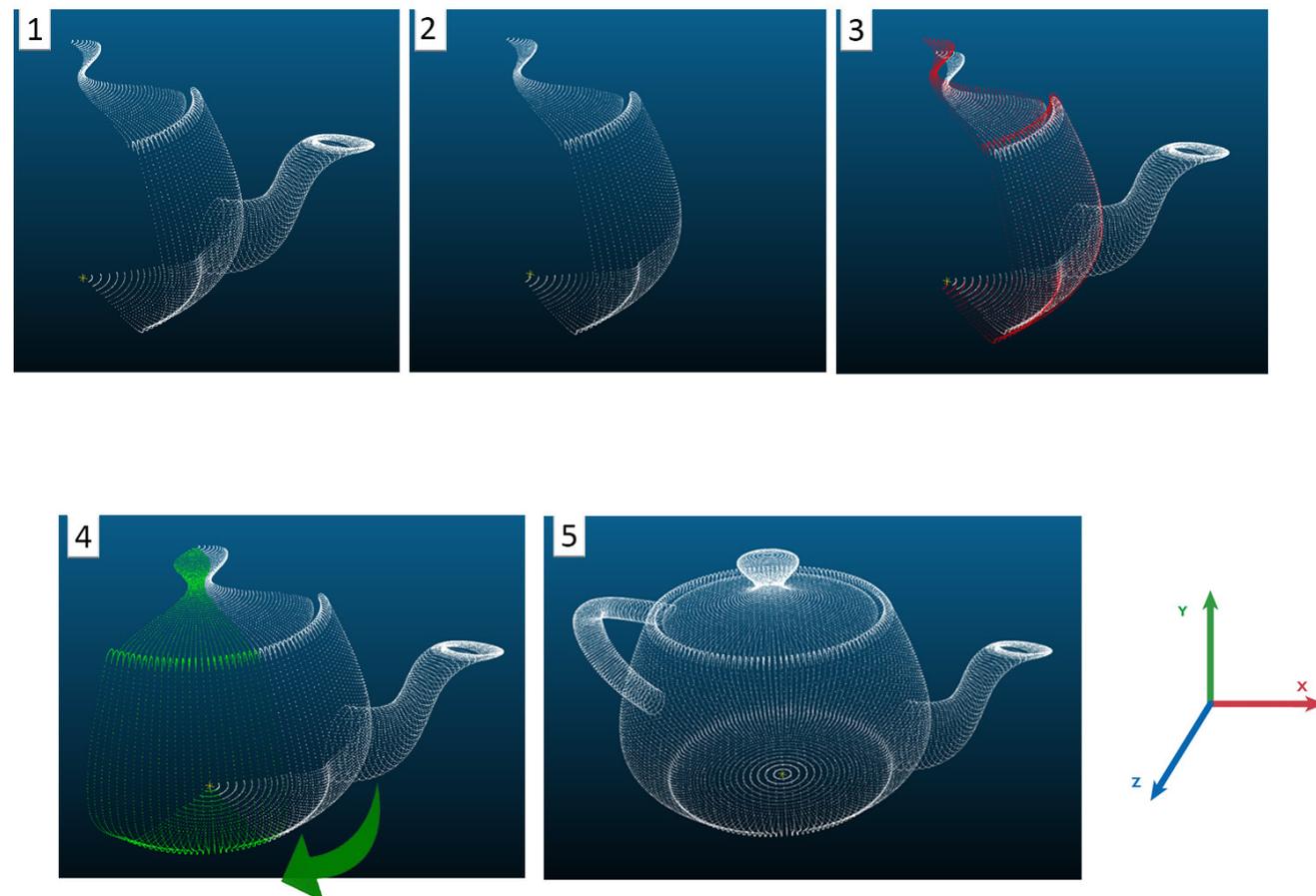
Figure 3. Steps to align the final. This is synthetic example assuming that the lidar is located in the center of the teapot point cloud

80   with β the angle of the motor, which depends on the time since the start of the scan and the rotation speed. Once all frames are assembled, the entire point cloud can be visualized.

As the VLP-16 Puck has the particularity of being able to scan continuously and at 360 degrees, two sets of symmetrical point clouds representing respectively the points with positive and negative coordinates on the x-axis of the lidar reference frame (see figure 5a) are created, which are theoretically superposed. This observation is a crucial point of the study as it

85   allows the calibrating of the system in order to maximize this superposition (the calibration procedure is described in section 3.2).

3.2 Calibration of the lidar system

Since out system is custom-assembled, there is little control on exact mounting angles, which therefore require calibration. Thus far, we have supposed that the system is turning around a fixed point corresponding to its optical center. In fact, given
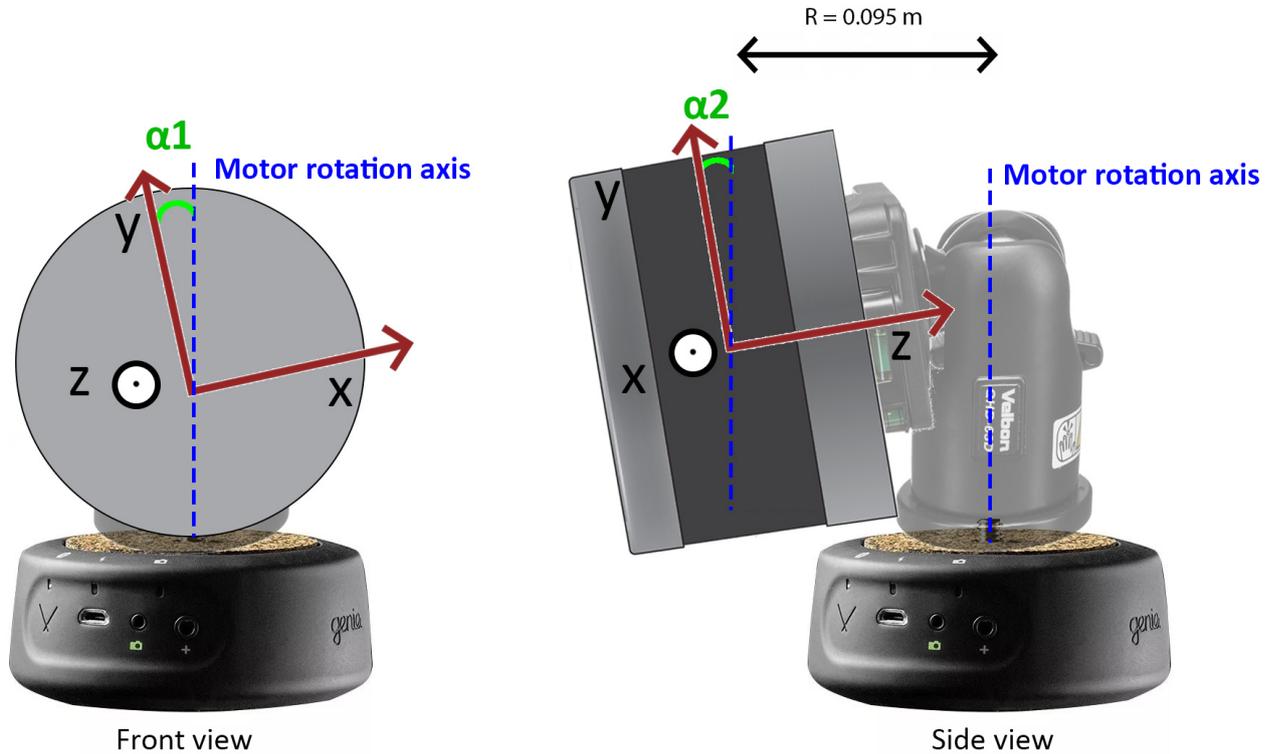
Figure 4. two possible angles between the system and the rotation axis

that the lidar is positioned on a ball head and a L-shaped liece, it is shifted from the rotation axis. This distance was manually measured as 0.095 m, and for each frame a translation on the z axis was applied. The affine transformation is a matrix presented as follows:

$$
T_2 = \begin{bmatrix} 1 & 0 & 0 & 0 \\ 0 & 1 & 0 & 0 \\ 0 & 0 & 1 & 0 \\ 0 & 0 & 0.095 & 1 \end{bmatrix}
$$

Another important consideration is that during the alignment of the frames, we have supposed that the Cartesian's coordinate system is the same as that of the motor. In fact, those two systems are different because the material is assembled by hand, which implies inaccuracies. Figure 4 shows the two possible angles α_1 and α_2 between the system and the rotation axis. The manual adjustment of those two systems involves an offset that highly influence the point cloud geometry if uncorrected. As these offsets cannot be measured manually, an automatic calibration is performed in post-treatment.

To find α_1 and α_2, the Nelder-Mead optimization algorithm is used, which is based on minimizing a continuous function using a simplex of dimensions equivalent to the number of parameters (Lagarias et al., 1998). At each iteration, a point located
100   near the initial simplex is generated involving a new sample if a minimum is found, until convergence.

The resolution of the densified scan is not regular. Indeed the point cloud resolution is very high near the lidar scanner and decreases away from the sensor. Because the algorithms for measuring the distance between two sets of point clouds require a lot of computer resources and must be repeated at each iteration of the Nelder-Mead optimization, the scans are downsampled to an uniform resolution. In addition, the optimization is carried out only for points within the distance range in the best accuracy range of 3 to 7 metres (Glennie et al., 2016).
105

The optimization seeks to obtain the α_1 and α_2 angles that minimize two functions:

1. During the rotation of the motor, the entire scene is recreated for each of the 16 scan lines. These identical images are then put back together to form a dense point cloud. The overlap of the images is influenced by changing the angle α_1. Thus, the function to be minimized corresponds to the average distance between all images produced by the scan lines 1 to 16.
110

2. The second function determines the angle α_2, based on the observation that both sets of symmetrical point clouds produced during the rotation must be exactly superposed. The variation of the angle α_2 creates a doming effect that tends to increase the average distance between both point clouds (figure 5). α_2 is determined by minimizing this distance.

115   **3.3   Effect of the calibration and performance of the system**

Visually, a wrong calibration of α_1 results in blur around the scanned image. A wrong calibration of the α_2 angle results in a doming effect that increases away from the center. To illustrate this, several scans were carried in a building of the University of Lausanne. A corridor of dimension 23 by 1.5 meters was scanned and a plan was fitted on the floor surface which is known to be horizontal. This plan is based on a distance interval to the lidar equivalent to the best accuracy range, i.e. between 3 and
120   7 meters depending on the lidar performance tests (Glennie et al., 2016). This avoids the influence of points too close or too far away, which can distort the theoretical equation of the plan. In addition, the points selected for fitting the plan come from an adequate sub-sampling of the initial scan in order to standardize the density of points over the distance interval. Then, the distance of all points to this theoretical plan are evaluated, which gives us an indication of the distribution of errors. Evaluation of the error as a function of the scanning distance was also measured.
125   Finally, a reproducibility test was performed for different motor speeds. The same scene was scanned several times to estimate the average distance between the point clouds. For that the Cloud to cloud Distance Tool with default parameters was performed in CloudCompare.

3.4 Testing the system in different environments

The system has been tested in various environments. For all scans performed, the Syrp Genie Mini has been configured to rotate
130   360 degrees in 6 minutes. These parameters allowed the acquisition of high points resolution to maximize the information
collected while maintaining a reasonable scan time. With this setting, about 10 millions points per scan are collected. The
first tests were carried out in a building of the University of Lausanne is characterized by vast surfaces and volumes. Then,
the system was then used in a confined environment with no available GNSS signal: the Baulmes mines, a limestone mine
disaffected at the end of the Second World War.

135   In these environments, several scans were assembled using the iterative closest point (ICP) alignment algorithm (Besl, P. J.,
McKay in 1992). This is the most popular method alignment approach for point clouds, which searches for nearest neighbors
to minimize the distance between two point clouds. Thus, several scans from different points of view are assembled into a
single point cloud without the use of GNSS.

3.5 Comparison with a high-cost system

140   The TLS was compared with an acquisition made with the ZEB-REVO from Geoslam. This system falls into the high-cost
category and can record 40,000 points per second and aligns them using a SLAM algorithm with an accuracy of 15 mm
according to manufacturers. This device has the advantage of not depending on a GPS connection for alignment, but is limited
by its range of only 30 meters. Thus, two scans representing the same scene were performed indoors with both systems. The
two scans were then registred in CloudCompare using the ICP algorithm (with default parameters). Then, the Cloudcompare
145   "Cloud to cloud distance" tool (with default parameters) was applied to measure the distance between the two point clouds.

4 Results

All point clouds are visualized in the CloudCompare software. An EDL (Eye Dome lighting) shading filter allowing the creation
of real-time shading has been applied for better visualization (CloudCompare, 2019).

4.1 Effects of calibration

150   Figure 5 shows the the quality of a scan that was carried out indoors in a work area of the University of Lausanne.

Figure 5a shows the scene after the alignment of the different frames produced by the VLP-16 during the scan. A kind of
blur caused by the splitting of the scene is observed. No processing has yet been done, so the parameters α_1 and α_2 are set to
0.

Figure 5b shows the scene after applying the calibration parameters defined using automatic calibration; however, a slight
155   blur is still present, which is caused by the overlapping of points from both halves of the lidar scan that are not perfectly
aligned.

Figure 5. Visualization of the calibration effects: (a) Scan without calibration, (b) Scan after calibration of α_1 and α_2, (c) Scan after post-treatment
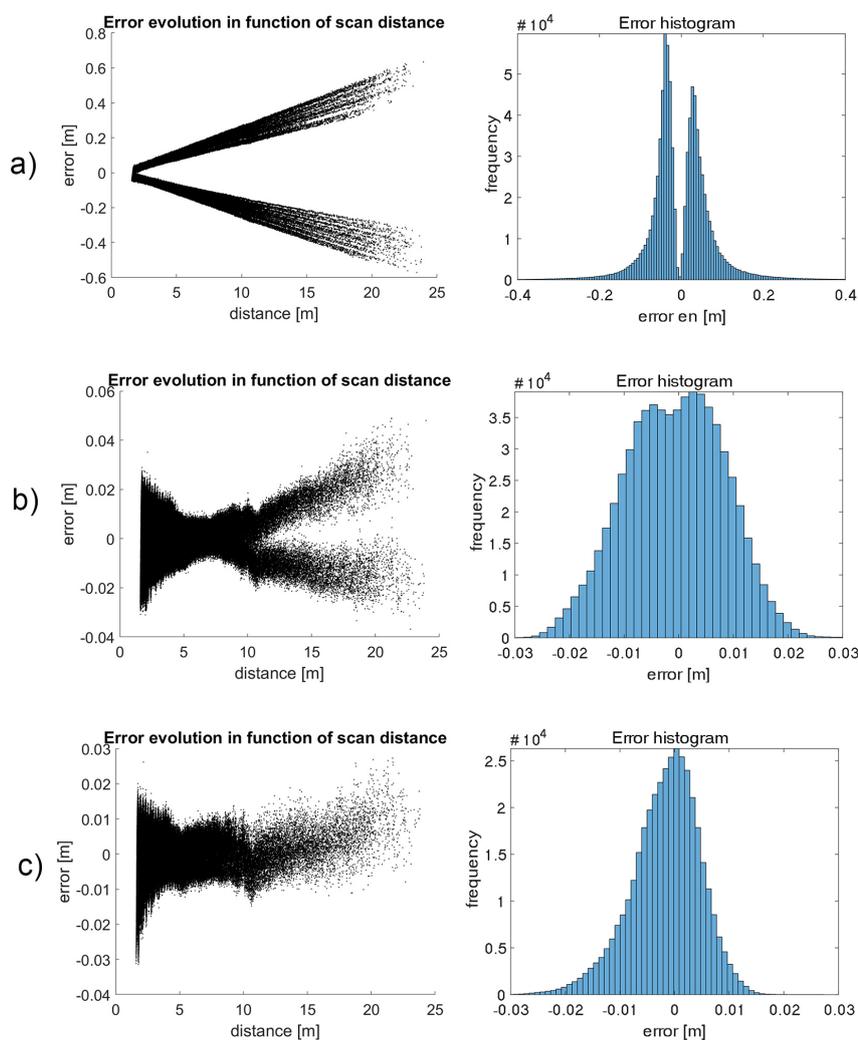
Figure 6. Effects of calibration in relation to a theoretical plan : (a) Error estimation before calibration, (b) Error estimation after calibration, (c) Error estimation after post-treatment

Figure 5c shows the scene where only the scanned points corresponding to the positives coordinates on the x-axis are displayed (i.e., 50% of the data are discarded). In addition, a sub-sampling at 0.005m is applying and a noise filtering is performed.

160   Figure 6 shows the error corresponding to the distance of the points from the theoretical plane and the error histogram for the three calibration steps respectively.

4.2 Densification quality

Figure 7a gives an overview of a scan performed indoors after calibration. A photograph of the scanned scene with the same viewing angle is shown in figure 7b

165   Figures 8a and 8b show two previews of scans performed at the Baulmes mines.

Figure 8c shows the result of the registration of 4 point clouds in the Baulmes mines. The points corresponding to each of the acquisitions are represented in a different color to highlight the registration. It should be noted that the clouds have not been cleaned to removed artifacts, so we can see that the sensor has scanned itself. The results are characterized by a spacing set at 0.005 meters and is visually realistic.

170   Table 3 shows the ability of the system to reproduce the same point cloud at four rotation speeds. For each speed, two scans were performed and the distance between them is evaluated. The average distance and standard deviation between all points are calculated.

Table 3. Reproducibility test for 4 scanning speed

Scan time	36s	1min	2min	6min
Mean distance [m]	0.0581	0.0167	0.0145	0.0108
Standard deviation [m]	0.169	0.0248	0.132	0.0343

To validate the registration, the calculation of the distances between the points coming from the assembly and those coming from GeoSLAM were done using CloudCompare with the option "Cloud to cloud distance". The average distance between

175   both point clouds and the standard deviations of these distances are shown in Table 4.

Table 4. Mean distance and Std. between the Geoslam and velodyne TLS

	Average distance [m]	Std. [m]
Before cleaning	0.0616	0.1991
After cleaning	<0.02	—

The calibration parameters for the indoors scans is shown in table 5. Table 6 shows the calibration parameters for the scans made in the Baulmes Mines.

Table 5. Summary of calibration parameters

Indoor scan	**Calibration α_1**	**Calibration α_2**
Scan 1	1.057	0.079
Scan 2	-0.631	0.347
Scan 3	-0.351	0.296
Scan 4	-1.061	-1.087

a)
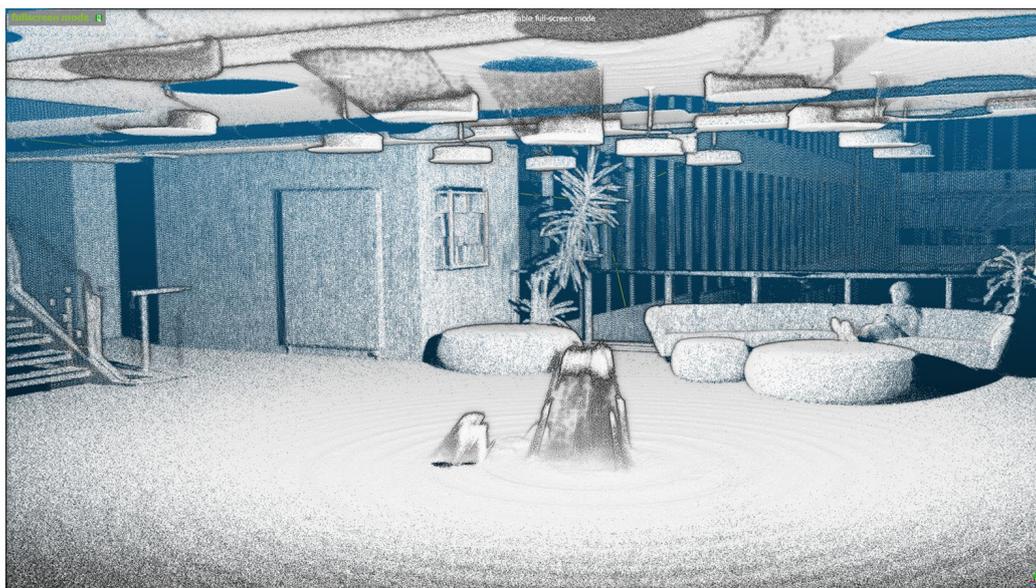
b)

Figure 7. Example of point cloud densification after calibration of the system : (a) Result of an indoor point cloud densification, (b) Picture of the scene
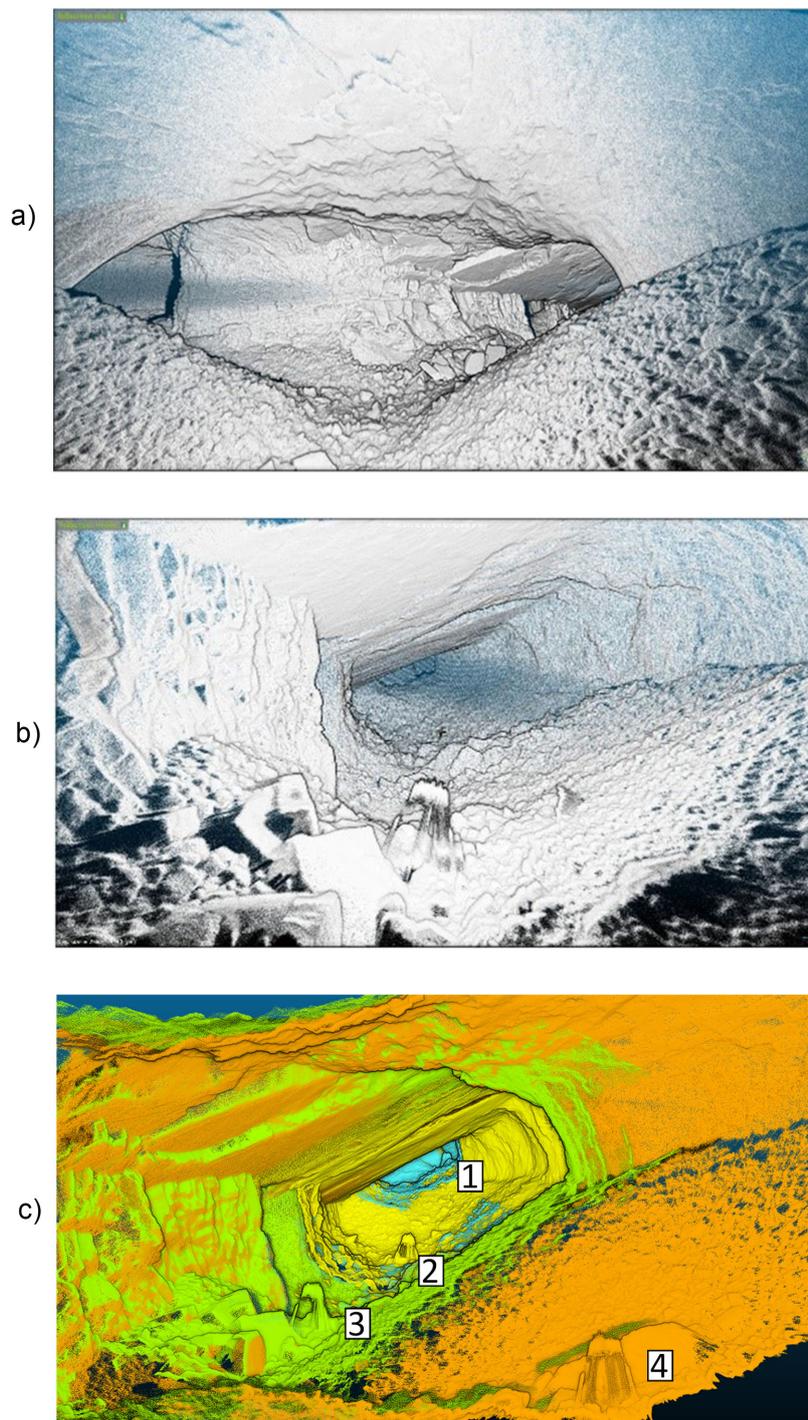
Figure 8. Scanned scenes in Baulmes mines. The height of the gallery is about 3.5 m : (a) Mine example 1, (b) Mine example 2, (c) Point cloud registration in the mine

Table 6. Summary of calibration parameters

Mines scan	Calibration α_1	Calibration α_2
Scan 1	-0.734	0.001
Scan 2	-1.279	-0.191
Scan 3	-1.313	-0.307
Scan 4	-1.164	-0.307
Scan 5	-0.704	-0.280

A close range artifact has been observed after the reconstruction of the scenes. Figure 9 illustrates this artifact, which is characterized by wavelets near the system that fade away with distance.

5 Discussion

5.1 Data analysis before and after calibration

As shown in Figure 5, calibration is a fundamental step in producing accurate 3D modeling of an environment.

The use of the two symmetrical datasets produced during an acquisition using the VLP-16 is a key element in the optimization of the system. However, as shown in Figure 5b, it is difficult to determine the calibration parameter accurately because it implies a slight deformation in the reconstruction of the point cloud. For this reason, we decided to keep only half of the points (Figure 5c) in order to obtain a sharper representation of the scene. This choice will be justified after the analysis of the following results.

The error depends on the distance to the lidar. Before calibration, the distance to the theoretical plane varies from about $\pm$ 4 cm for the closest points to the lidar to 59 cm for a scan distance of 23 m (figure 6a). After calibration of parameters α_1 and α_2, the entire point cloud approaches the theoretical surface, as shown in Figures 6b. However the evolution of the error as a function of distance is still not constant, being about $\pm$ 2.5 cm for the points closest to the lidar, dropping to about $\pm$ 1 cm at a distance of 7.5 m, and eventually reaching $\pm$ 4 cm for a scan distance of 23 m. The minimum error is logically in the point range where the theoretical plan is situated. The bimodal error histogram shown in fibure 6b and (centred at $\pm$ 0.5 cm) shows that the superposition between the two halves of the scan is still not entirely accurate despite the calibration performed.

The evolution of the error as a function of the scanning distance when keeping only the half of the scan (figure 6c) shows an accuracy range of $\pm$ 2.5 cm, which remains within the accuracy range proposed by Velodyne.

5.2 Performance and stability of the TLS

According to the manufacturer's website, the VLP-16 Puck allows data acquisition at a distance of 100 m for an accuracy of $\pm$ 3 cm, under optimal acquisition conditions. Various stability tests have been carried out in metrology laboratory, which indicate an accuracy of $\pm$ 2 cm for an acquisition distance of 5 meters to a white and flat target (Glennie, et al., 2016). The
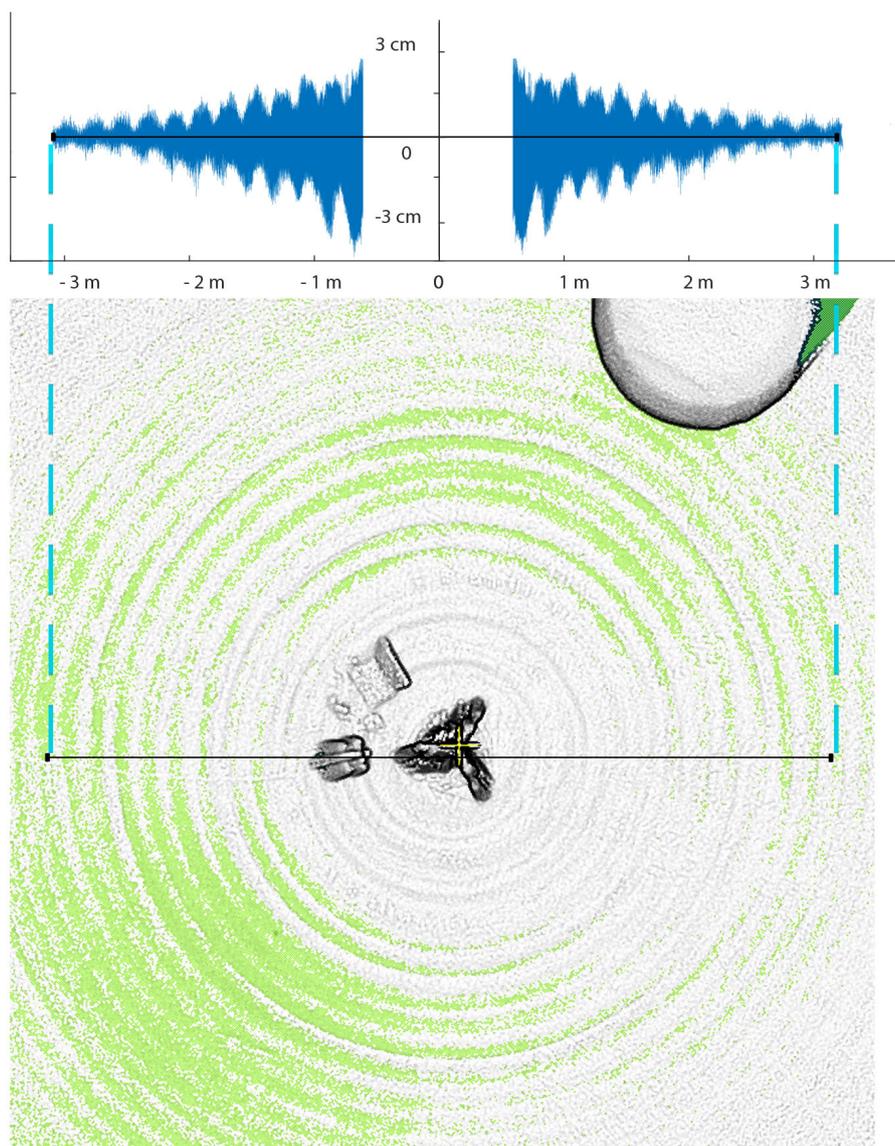
Figure 9. Artifact present near the TLS and its corresponding amplitude

tests carried out during this study made it possible to evaluate the performance of the lidar against a theoretical plan produced using a scanned flat surface (the central corridor of a building).

Reproducibility tests of the measurements made for scan speeds ranging from 36 seconds to 6 minutes show us that the motor speed must be as low as possible to increase the quality of the measurements.

205 The post-processing steps and the calibration of mounting angles has allowed to drastically reduce errors; however, the calibration parameters vary greatly between scans, as shown in table 5 and table 6. This can be explained by the assembly of our lidar system being relatively unstable. The impact of the calibration, and particularly the need to repeat the calibration for each scan, could be alleviated by welding together the different components of the system.

5.3 Comparison with more expensive hardware

210 The generation of dense and accurate scans allowed the use of an ICP algorithm for point clouds registration. After comparing the scans performed with the Geoslam, superposition of ± 2 cm is present, which shows that the two scans overlap well. Some areas where the distance between the two scans is more than 10 cm correspond to the presence of people during the acquisition with GeoSLAM (table 6).

5.4 Origin of the short-range artifacts

215 Visually, this artifact is easily observed in the results of scans near the tripod,when data acquired on a flat surface. Figure 9 shows the influence of this artifact on the scan. We notice that the error spreads in the form of regular waves and fades away as it moves away from the lidar. It has a magnitude of 3 cm at the closest to the lidar and drops below 1.5 cm at a distance of 3m. The wave frequency is about 20cm. A hypothesis on the origin of this artifact would be related to the length of the arm which was measured manually. After various tests, it turns out that errors in the length of the arm has no influence on the

220 occurrence of these artifacts, but instead creates horizontal deformations. Another hypothesis is that the artifacts are related to the scanning speed of the lidar system. However, the artifacts remain constant (same distance and amplitude between waves) despite changes in engine rotation speeds. This tells us that the artifacts seem to be related to the lidar itself. Since the error appears to be regular, it would be conceivable to correct outliers by modifying each point according to the distance to the lidar.

6 Conclusion

225 As shown in the results, our system requires calibration for each scan performed. Optimization of the equipment, such as the use of a more accurate engine, is possible for such a project and could improve the quality of the measurements while maintaining a low-cost aspect. The results obtained with this system are satisfactory. The use of the lidar system in a mine has proven its ability to be independent of a GPS referencing system. Comparison with a high-cost system using a SLAM alignment algorithm verified the quality of registration. A follow-up to this study could be the validation of the performance

230 of this system using a total station survey. The use of this lidar system on mobile supports is possible with the addition of an inertial station. This study has shown that TLS allows high and accurate data production can be used at a lower cost.

Code availability. Velodyne TLS

GitHUB repository

Data availability.

235 *Code and data availability.*

Sample availability.

Video supplement.

Baulmes

Reclere

240 Milandre

Rolex Learning Center

Appendix A

A1

Author contributions. JB developed the methodology, carried out the field experiments and wrote the manuscript, MHD provided advice and
245 methodological guidance and contributed to the manuscript, GM proposed the initial framework, provided supervision and contributed to the
manuscript

Competing interests.

Disclaimer.

Acknowledgements. We thank Stephane Affolter, Pierre-Xavier Meury and Eric Gigandet for access to caves for testing our method

250 **References**

Ackermann, F.: Airborne laser scanning—present status and future expectations, ISPRS Journal of Photogrammetry and Remote Sensing, 54(2–3), 64–67, doi:10.1016/S0924-2716(99)00009-X, 1999.

Barnea, S. and Filin, S.: Keypoint based autonomous registration of terrestrial laser point-clouds, ISPRS Journal of Photogrammetry and Remote Sensing, 63(1), 19–35, doi:10.1016/j.isprsjprs.2007.05.005, 2008.

255 Davis, P. A.: The Analysis of Lidar Signatures of Cirrus Clouds, Appl. Opt., 8(10), 2099, doi:10.1364/AO.8.002099, 1969.

Geiger, A., Lenz, P. and Urtasun, R.: Are we ready for autonomous driving? The KITTI vision benchmark suite, in 2012 IEEE Conference on Computer Vision and Pattern Recognition, pp. 3354–3361., 2012.

Glennie, C. L., Kusari, A. and Facchin, A.: Calibration and stability analysis of the VLP-16 laser scanner, Int. Arch. Photogramm. Remote Sens. Spatial Inf. Sci., XL-3/W4, 55–60, doi:10.5194/isprs-archives-XL-3-W4-55-2016, 2016.

260 Jaboyedoff, M., Oppikofer, T., Abellán, A., Derron, M.-H., Loye, A., Metzger, R. and Pedrazzini, A.: Use of LIDAR in landslide investigations: a review, Nat Hazards, 61(1), 5–28, doi:10.1007/s11069-010-9634-2, 2012.

Lagarias, J. C., Reeds, J. A., Wright, M. H. and Wright, P. E.: Convergence Properties of the Nelder–Mead Simplex Method in Low Dimensions, SIAM J. Optim., 9(1), 112–147, doi:10.1137/S1052623496303470, 1998.

Laurent, A., Moret, P., Fabre, J. M., Calastrenc, C., Poirier, N.: La cartographie multi-scalaire d'un habitat sur un site accidenté: la Silla del
265 Papa (Espagne), 2019.

Mada, S. K., Smith, M. L., Smith, L. N. and Midha, P. S.: Overview of passive and active vision techniques for hand-held 3D data acquistion, edited by A. Shearer, F. D. Murtagh, J. Mahon, and P. F. Whelan, pp. 16–27, Galway, Ireland., 2003.

Northend, C. A., Honey, R. C. and Evans, W. E.: Laser Radar (Lidar) for Meteorological Observations, Review of Scientific Instruments, 37(4), 393–400, doi:10.1063/1.1720199, 1966.

270 Pouliot, J.: GMT-7006: Modelisation et Geovisualisation 3D. Universite Laval, departement des sciences geomatiques, 2018.

Royán, M. J., Abellán, A., Jaboyedoff, M., Vilaplana, J. M. and Calvet, J.: Spatio-temporal analysis of rockfall pre-failure deformation using Terrestrial LiDAR, Landslides, 11(4), 697–709, doi:10.1007/s10346-013-0442-0, 2014.

Schuster, B. G.: Detection of tropospheric and stratospheric aerosol layers by optical radar (Lidar), Journal of Geophysical Research (1896-1977), 75(15), 3123–3132, doi:10.1029/JC075i015p03123, 1970.

275 Shackleton, J., VanVoorst, B. and Hesch, J.: Tracking People with a 360-Degree Lidar, in 2010 7th IEEE International Conference on Advanced Video and Signal Based Surveillance, pp. 420–426., 2010.

Shan, J. and Toth, C. K.: Topographic laser ranging and scanning: principles and processing, Second edition., Taylor Francis, CRC Press, Boca Raton., 2018.

Stöcker, C., Nex, F., Koeva, M. and Gerke, M.: Quality assessment of combined IMU/GNSS data for direct georeferencing in the context of
280 UAV-based mapping, Int. Arch. Photogramm. Remote Sens. Spatial Inf. Sci., XLII-2/W6, 355–361, doi:10.5194/isprs-archives-XLII-2-W6-355-2017, 2017.

Teza, G., Galgaro, A., Zaltron, N. and Genevois, R.: Terrestrial laser scanner to detect landslide displacement fields: a new approach, International Journal of Remote Sensing, 28(16), 3425–3446, doi:10.1080/01431160601024234, 2007.

Wang, Z., Liu, Y., Liao, Q., Ye, H., Liu, M. and Wang, L.: Characterization of a RS-LiDAR for 3D Perception, in 2018 IEEE 8th Annual
285 International Conference on CYBER Technology in Automation, Control, and Intelligent Systems (CYBER), pp. 564–569, IEEE, Tianjin, China., 2018.